IBRACON Structures and Materials Journal
Revista IBRACON de Estruturas e Materiais
ISSN 1983-4195 ismj.org

ORIGINAL ARTICLE

Analytical and numerical investigation of deflections in UHPFRC beams under four-point bending

Investigação analítica e numérica de deflexões em vigas de UHPFRC sujeitas à flexão em quatro pontos

Felipe Augusto da Silva Barbosa[a]
Antonio Domingues de Figueiredo[b]
Ramoel Serafini[c]
Ricardo Carrazedo[d]
Luís Antônio Guimarães Bitencourt Júnior[a]

[a]Universidade de São Paulo, Departamento de Engenharia de Estruturas e Geotécnica, São Paulo, SP, Brasil
[b]Universidade de São Paulo, Departamento de Engenharia de Construção Civil, São Paulo, SP, Brasil
[c]Universidade São Judas Tadeu, Departamento de Engenharia Civil, São Paulo, SP, Brasil
[d]Universidade de São Paulo, Departamento de Engenharia de Estruturas, São Carlos, SP, Brasil

Received 04 July 2025
Revised 09 October 2025
Accepted 24 November 2025

Abstract: UHPFRC is a composite material characterized by its high strength, ductility, and durability. However, estimating deflections in UHPFRC beams is challenging due to the material's pronounced nonlinearity, which makes it difficult to apply conventional elastic analysis methods directly. Thus, this paper presents the development of an analytical method for calculating the load-deflection curves of reinforced UHPFRC beams subject to four-point bending. The methodology is based on cross-sectional equilibrium and compatibility to determine the curvatures along the beam, which are subsequently integrated using the principle of virtual work to obtain the deflections. The proposed approach is validated by comparing the results with experimental data from literature and with a finite element analysis performed in this study. The analytical method showed good agreement with the experimental results and exhibited strong agreement with the finite element simulations, particularly at service load levels.

Keywords: UHPFRC, load-deflection, moment-curvature, analytical method, FEM analysis.

Resumo: O UHPFRC é um material compósito caracterizado por sua elevada resistência, ductilidade e durabilidade. No entanto, a estimativa das flechas em vigas de UHPFRC apresenta desafios significativos devido à acentuada não linearidade do material, o que dificulta a aplicação direta dos métodos convencionais de análise elástica. Assim, este artigo descreve o desenvolvimento de um método analítico para o cálculo das curvas carga–flecha de vigas de UHPFRC armadas submetidas à flexão em quatro pontos. A metodologia baseia-se no equilíbrio e na compatibilidade da seção transversal para determinar as curvaturas ao longo da viga, que são posteriormente integradas pelo princípio dos trabalhos virtuais para obter as flechas. A abordagem proposta é validada por meio da comparação com resultados experimentais da literatura e de uma análise numérica por elementos finitos realizada neste estudo. O método analítico apresentou boa concordância com os resultados experimentais e excelente correlação com as simulações numéricas, especialmente em níveis de carregamento de serviço.

Palavras-chave: UHPFRC, carga-deflexão, momento-curvatura, método analítico, MEF.

How to cite: F. A. S. Barbosa, A. D. Figueiredo, R. Serafini, R. Carrazedo, L. A. G. Bitencourt Jr., "Analytical and numerical investigation of deflections in UHPFRC beams under four-point bending," *Rev. IBRACON Estrut. Mater.*, vol. 18, no. 6, e18606, 2025, https://doi.org/10.1590/S1983-41952025000600006

Corresponding author: Luís Antônio Guimarães Bitencourt Júnior. E-mail: luis.bitencourt@usp.br

Financial support: Felipe A.S. Barbosa acknowledges that this study was financed in part by the *Coordenação de Aperfeiçoamento de Pessoal de Nível Superior* - Brazil (CAPES) - Finance Code 001. Antonio D. de Figueiredo gratefully acknowledges CNPq for the support (Grants #305673/2023-8 and #404254/2023-3). Ramoel Serafini would like to thank the São Paulo Research Foundation (FAPESP) for the Regular Research funding (Grant #2022/14045-5). Ricardo Carrazedo acknowledges CNPq for the support (Grant #316138/2023-1). Luís A.G. Bitencourt Jr. would also like to extend his acknowledgments to the financial support of CNPq (Grant #307175/2022-7) and FAPESP (Grant #2022/03179-0).

Conflict of interest: Nothing to declare.
Data Availability: The data that support the findings of this study are available from the corresponding author upon reasonable request.

1 INTRODUCTION

Ultra-high-performance fiber-reinforced concrete (UHPFRC) may provide a significant advancement over conventional concrete, relying on its superior mechanical properties and durability. Whereas conventional concrete exhibits low tensile strength and is prone to cracking, the dense microstructure of UHPFRC, combined with the incorporation of fibers, results in elevated compressive and tensile strengths, thereby enabling the construction of more slender, ductile, and durable structural elements [1]. However, UHPFRC technology is still under development, and some aspects, such as the consideration of fiber orientation in design models, still lack a consensus approach [2], [3].

One of the most critical aspects of structural design is accurately predicting deflections under various loading conditions, which must account for the multiple stages of material deformation. For traditional reinforced concrete (RC), deflections are typically computed using analytical methods based on elastic analysis, in which the effects of cracking and reinforcement are represented by the variations in the effective member stiffness [4].

Yoo *et al.* [5] developed equations to predict the cracked moment of inertia and estimate the service deflections of UHPFRC members with non-metallic reinforcement using Branson's Equation [6]. Gao *et al.* [7] applied the same principles to calculate the effective moment of inertia, considering the fibers separately from the concrete matrix and modeling them as uniformly distributed reinforcements across the height of the structural element. However, Branson's effective inertia may not fully represent the stiffness variation across the member. The phenomenon of strain hardening-softening makes the tensile stress-strain relationship highly nonlinear, leading to different cracking patterns and stress distribution compared to traditional RCs. Moreover, studies ([8], [9] and [10]) have shown that the presence of fibers provides significantly higher post-cracking stiffness to UHPFRC beams, slowing the widening of cracks, which is a phenomenon not considered by conventional methods.

Peng *et al.* [11] also attempted to develop a procedure that accounts for the UHPFRC tensile behavior in calculating the effective moment of inertia. An idealized moment-curvature relationship was established to compute midspan deflections through numerical integration. However, the applicability of this method is limited to small load levels, up to 1.2 times the cracking load or 0.5 times the ultimate load, for which it was experimentally validated. Thus, the complete load-deflection curve, including the descending portion, was not obtained, and the tensile softening effect on the overall flexural behavior was not evaluated.

Given the challenges in predicting flexural behavior using analytical methods, finite element modeling remains a valuable alternative for UHPFRC structural members. Nonetheless, the input data associated with the softening branch of the tensile constitutive model is mesh-sensitive [12], leading to inaccurate results if it is not correctly adjusted. Moreover, FEM software requires numerous parameters that may not even influence the results of the analysis. This makes the process time-consuming, especially for those with limited experience in FEM modeling, whose primary goal is to accurately predict the flexural behavior and perform parametric analysis for structural design purposes.

To overcome the shortcomings of existing approaches, this paper presents and experimentally validates an analytical procedure for determining the complete load-deflection curves of reinforced UHPFRC beams under four-point bending. Unlike previous research, the proposed method, based on cross-sectional analysis, accounts for stiffness variation from point to point rather than calculating average moments of inertia. The curvatures are determined at each node where the structural element is discretized, based on a moment-curvature relationship that captures the full material behavior in both compression and tension. Subsequently, the deflection is computed at any node of the beam employing the principle of virtual work.

This study aims to investigate the serviceability behavior of UHPFRC structural members by evaluating their ductility and computing the loads and deflections that define the onset of cracking, reinforcement yielding and failure. In addition, the analytical load-deflection curves are compared with those obtained experimentally and through FEM analysis, providing a comprehensive assessment of the proposed methodology.

2 METHODOLOGICAL APPROACHES

The proposed analytical procedure, detailed in subsection 2.1, was computationally implemented in-house using MATLAB language. The results of four-point bending tests conducted by Yang *et al.* [13] are used to validate the model. The procedures for the experimental validation are described in subsection 2.2. Finally, the assumptions for finite element modeling are presented in subsection 2.3.

2.1 Analytical approach

The analytical procedure is based on the principle of virtual work, according to which the work performed by virtual external forces under the actual compatible displacement must equal the strain energy stored in the structure due to virtual internal forces [14]. Accordingly, the calculation of displacements begins with determining the cross-sectional curvatures φ(x) and distortions γ(x) along the beam.

The static problem is solved by longitudinally discretizing the beam into segments of length Δx. For each node, the actual deformation parameters φ and γ, as well as the internal virtual forces and moments, are determined. As described by the Equation (1), the vertical displacement δ at a given point is found by ensuring that the work done by a vertical virtual force $\bar{F}$ applied at that point equals the work done by the internal virtual shear forces $\bar{V}$ and bending moments $\bar{M}$, with respect to the actual deformed configuration.

$$\bar{F}\delta = \int_{D_L} \bar{V}(x)\gamma(x)dx + \int_{D_L} \bar{M}(x)\varphi(x)dx \tag{1}$$

The shear strain γ is computed using Equation (2), where G_{cm} and A_c refer to the shear modulus of elasticity and the cross-sectional area, respectively. The shear force *V(x)* relates to the actual loading, while the parameter f_{sh} corresponds to the shape factor for shear, taken as 1.2 in accordance with [15]. As indicated by Equation (3), the modulus G_{cm} derives from the longitudinal modulus E_{cm} and Poisson's ratio ν, which is assumed to be 0.2 due to the lack of experimental data.

$$\gamma(x) = \frac{V(x)}{G_{cm}A_c / f_{sh}} \tag{2}$$

$$G_{cm} = \frac{E_{cm}}{2(1+\upsilon)} \tag{3}$$

Accordingly, all the parameters required to calculate the first integral I_{n1} of Equation (6) are established. To compute the second integral over the beam domain D_L, the curvatures φ are derived from the moment-curvature *M-φ* relationship obtained through cross-section analysis, for which the stress and strain diagrams are illustrated in Figure 1.

The cross-section is divided into *n* rectangular segments of thickness *dh*, each located at a distance y_i from the upper face. The stress on the middle of each segment σ_{ci} derives from the constitutive relations of the material, using the strain ε_{ci} obtained from Equation (4). The terms ε_t and x_c denote the strain at the top fiber and the depth of the neutral axis, respectively.

$$\varepsilon_{ci} = \varepsilon_t (y_i - x_c) / x_c \tag{4}$$

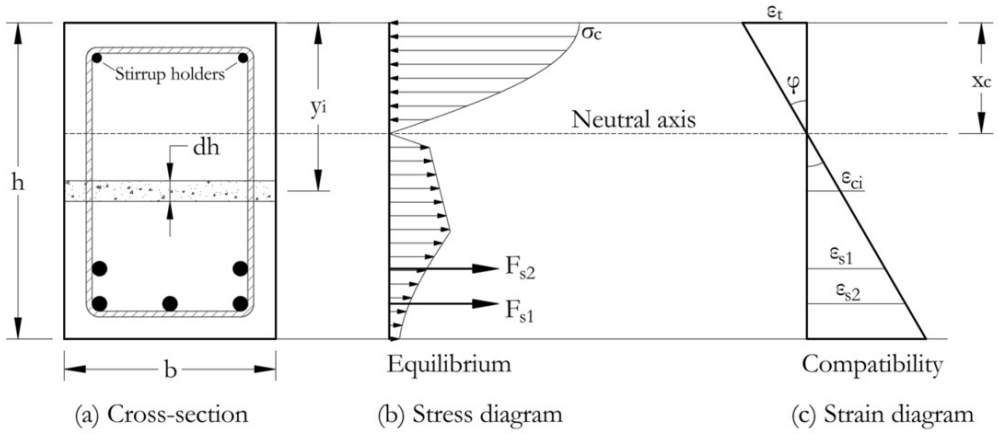

Figure 1 – Equilibrium of forces and strain compatibility to compute the moment-curvature relationship

Since the negative moments at the supports are negligible, ε_t does not need to reach excessively high tensile strain levels. Therefore, ε_t is varied from the cracking strain $-\varepsilon_{t1}$ to the crushing strain ε_{cu1f}. The neutral axis depth x_c is determined iteratively, ensuring equilibrium such that the sum of all sectional forces equals zero. Once the equilibrium condition is achieved, the resulting bending moment *M* is calculated as in Equation (5). The first summation represents

the contribution of each concrete segment (area Aci), while the second accounts for the reinforcement layers (area A_{sj}), located at distance y_j from the upper face. The curvature φ associated with M corresponds to the ratio between ε_t and x_c.

$$M = \sum_{i=1}^{n} \sigma_{ci} A_{ci} \left(y_i - x_c \right) + \sum_{j=1}^{n_s} \sigma_{sj} A_{sj} \left(y_j - x_c \right) \tag{5}$$

Figure 2 presents a typical M-φ relationship for a rectangular cross-section of a reinforced UHPFRC beam. Points A and C correspond to loading conditions that cause excessive tension or compression, while peak B represents the maximum moment the beam can withstand. Figure 3 shows the diagram of curvatures φ(x), obtained by interpolating the nodal moments $M(x)$ onto the M-φ relationship.

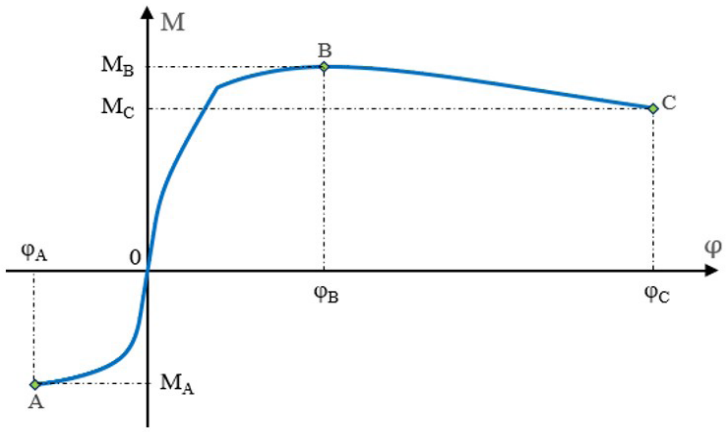

Figure 2 – Typical moment-curvature relationship for a reinforced UHPFRC beam

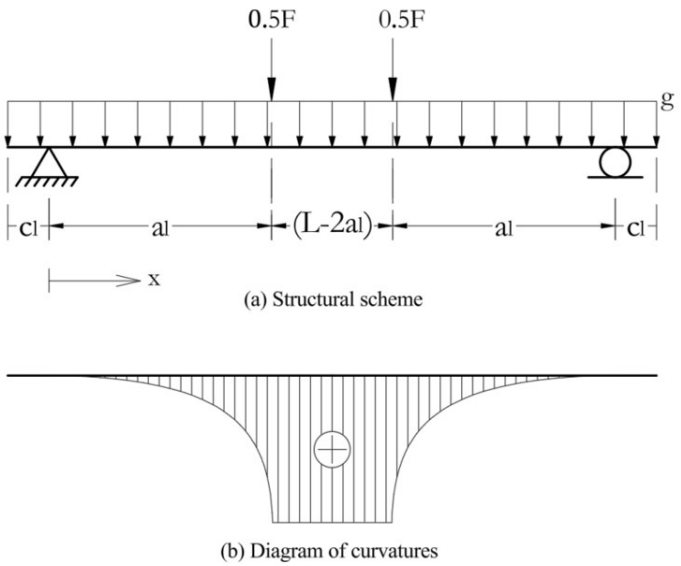

Figure 3 – Structural scheme (a) and diagram of curvatures (b) for the beam under four-point bending

As the midspan moment increases without exceeding M_B, the curvature φ(x) at any beam section is derived from the ascending branch AB of the M-φ curve. Once the peak is surpassed, the curvatures in the shear spans continue to follow AB, whereas those at midspan are determined from the descending branch BC.

After obtaining the nodal curvatures φ and the virtual moments $\bar{M}$, the next step is to calculate In_2, the second integral in Equation (1). The values of φ and $\bar{M}$ within each element of length Δx are determined by linear interpolation between nodal values, as illustrated in Figure 4. This same procedure can be applied to compute the first integral In_1, provided that $\bar{V}$ and γ are known at the nodes.

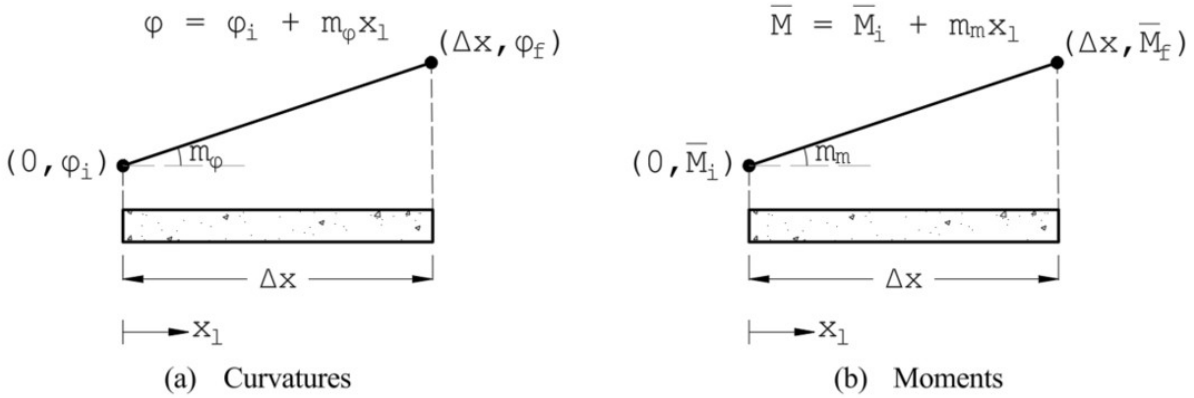

Figure 4 – Determination of the linear interpolation functions with respect to the element's local coordinate systems

The slopes *m* of the interpolation functions can be determined geometrically, based on the nodal coordinates and the element length Δx. Summing the contribution of all discretization elements, the displacement δ at the point and direction of $\bar{F}$ is obtained as follows:

$$\delta = \frac{1}{\bar{F}} \left\{ \sum_{i=1}^{n_{el}} \left[\int_0^{\Delta x} (\gamma_i + m_\gamma x_l)(\bar{V}_i + m_v x_l) dx_l + \int_0^{\Delta x} (\varphi_i + m_\varphi x_l)(\bar{M}_i + m_m x_l) dx_l \right] \right\} \tag{6}$$

The constitutive relations adopted for the cross-section analysis follow the French standard NF P 18-710 [16]. In compression, the stress-strain relationship is given by Equation (7) (Figure 5.a), where $\varepsilon_{c1,f}$ denotes the strain at peak stress. Parameters η and ϕ are obtained according to Section 3.1.5 of the reference code, based on the compressive strength f_{cm} and the modulus E_{cm}.

$$\sigma_c = f_{cm} \left[\frac{\eta \left(\varepsilon / \varepsilon_{c1,f} \right)}{\eta - 1 + \left(\varepsilon / \varepsilon_{c1,f} \right)^{\Phi \eta}} \right] \tag{7}$$

The global fiber orientation factor K_{global}, required for $\varepsilon_{c1,f}$ and $\varepsilon_{cu1,f}$, was calibrated to match stress-strain curves from uniaxial compression tests reported in [13]. Calibration ensured a nearly linear ascending branch, so K_{global} was iteratively adjusted until $\varepsilon_{c1,f}$ and σ_c converged to f_{cm}/E_{cm} and f_{cm}, respectively.

For tension, Figure 5.b illustrates the adopted stress-strain relation, divided into elastic, hardening, and softening stages. The elastic strain ε_{el} is obtained by f_t/E_{cm}, where by f_t is the cracking strength The peak tensile strain $\varepsilon_{t,max}$ is determined using Equation (8), with characteristic length l_c assumed as 2/3 of the cross-section height *h* [16].

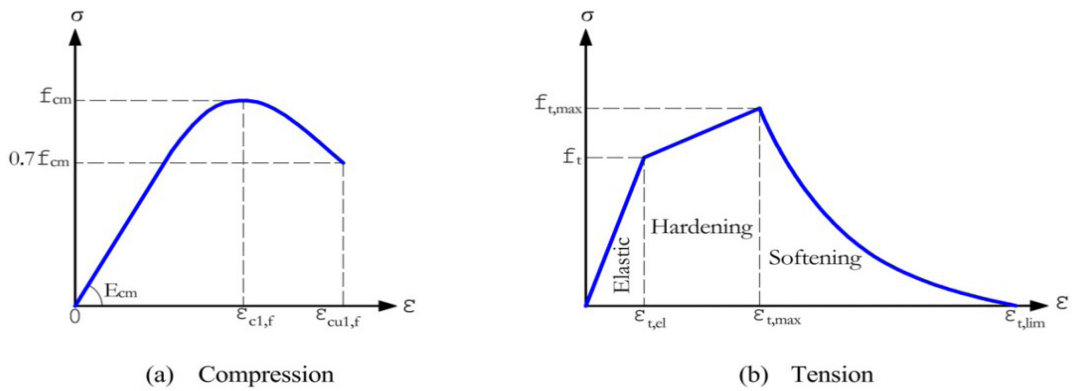

Figure 5 – Adopted constitutive models – Adapted from [16]

The σ-ε relationship during the softening was derived from σ-*wcr* curves obtained through inverse analysis of three-point bending tests. Equation (9) converts crack opening displacement w_{cr} into the strain ε. Unlike the standard [16],

this study discretizes the post-peak σ-ε curve into multiple points, providing an exponential rather than linear/bilinear representation, and thus more realistically capturing softening.

$$\varepsilon_{t,max} = min\left(\frac{l_f}{4l_c}, 0.004\right) \tag{8}$$

$$\varepsilon = \varepsilon_{t,max} + \frac{w_{cr}}{l_c} \tag{9}$$

For the reinforcement, a bilinear stress-strain model was adopted (Figure 6). Linear elasticity applies for $0 \leq \varepsilon < \varepsilon_y$ while linear hardening governs stresses beyond f_y in both tension and compression.

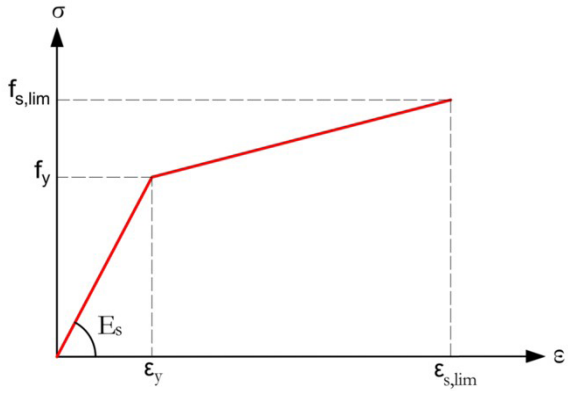

Figure 6 – Bilinear stress-strain diagram for steel

2.2 Experimental Validation

To validate the analytical procedure, the load-deflection curves of beams tested by Yang *et al.* [13] were computed and compared to the experimental curves.

Cross-sections were discretized into 1 mm segments. The top strain ε_t was divided into increments $\Delta\varepsilon_t \approx 10^{-5}$, generating a vector with 1001 elements to capture nonlinearities in the M–φ relation.

Table 1 summarizes the geometry, reinforcement, and casting procedures of the 14 beams tested, along with batch identification. Non-reinforced beams are designed NR, while reinforced beams follow the notation Rxy, where x = number of layers and y = rebars per layer. Duplicate specimens are labeled "1" and "2". Casting procedures are denoted "End" (casting from supports to midspan) or "Midspan" (casting from midspan to supports).

Table 1 – Details of the specimens tested by Yang et al. - Adapted [13]

Beam	**NR-1,2**	**R12-1,2**	**R13-1,2**	**R13C-1,2**	**R14-1,2**	**R22-1,2**	**R23-1,2**
Cross-section	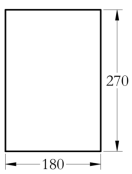	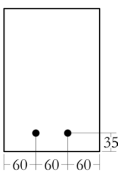	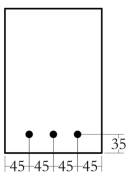	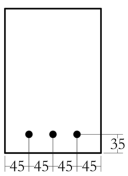	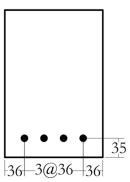	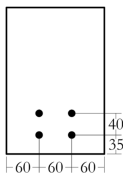	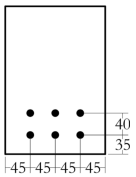
A_σ (mm²)	-	253.4	380.1	380.1	506.8	506.8	760.2
Placing	End	End	End	Midspan	End	End	End
Batch	4	1	2	2	3	1	3

UHPFRC properties for the four batches are listed in Table 2. Compressive strength f_{cm} and modulus E_{cm} were obtained from uniaxial compression, while flexural strength f_f was measured from three-point bending tests on notched square prisms (100 x 100 mm² cross-section, clear span of 300 mm and notch 10 mm high).

The stress-crack opening σ-w_{cr} curve was obtained from the results of the three-point bending tests, applying the inverse analysis method proposed by Lee *et al.* [17], whereby the idealized failure mode of the test and the cross-sectional analysis are illustrated in Figure 7.

Table 2 – Mechanical properties measured by Yang *et al.* [13] for all batches

Material Properties	Batch 1	Batch 2	Batch 3	Batch 4
Compressive strength f_{cm} (MPa)	190.9	192.2	196.1	196.7
Modulus of elasticity E_{cm} (MPa)	46,418	46,680	45,530	46,818
Equivalent flexural stress f_f (MPa)	30.9	29.4	29.3	32.7

In summary, the method involves adjusting one of the parameters associated with the σ-w_{cr} curve, so that the maximum numerical load supported by the prism P_{num} matches its experimental counterpart P_{exp}. The experimental load P_{exp} is calculated from the equivalent flexural strength f_f, according to Equation (10), where b is the prism width and h_t is the difference between its total height and the notch depth.

$$P_{exp} = \frac{2}{3}\left(\frac{bh_t^2}{L}\right) \tag{10}$$

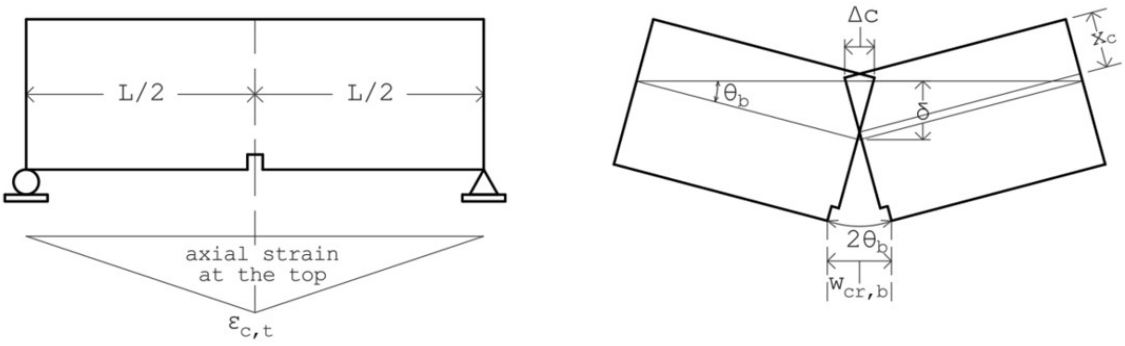

Figure 7 – Idealized failure mode to predict the σ-$w_{\chi\rho}$ curve from the results of three-point bending tests – Adapted from [17]

The load P_{num} is obtained from the maximum bending moment that the notched section can withstand for a given σ-w_{cr}. The crack opening at the bottom $w_{cr,b}$ is assumed to vary from 0 to a threshold value $w_{cr,lim}$, which indicates the complete loss of the element's capacity to resist the applied loads. Since failure is governed by fiber pullout, $w_{cr,lim}$ is taken as half of the fiber length $l_f/2$.

During compression and before cracking, both the concrete matrix and the fibers are considered as a single material, with the total stress σ_c computed elastically, as a function of the strains ε_{ci} at different locations of the cross-section. These strains are calculated using the geometrical conditions illustrated in Figure 8 and expressed by Equation (11):

$$\varepsilon_{ci} = \frac{2}{L}\left(\frac{y_i - x_c}{h_t - x_c}\right) w_{cr,b} \tag{11}$$

Upon exceeding the cracking strength f_t, the stresses in the matrix σ_{mat} and fibers σ_{fib} were calculated separately using Equations (12) and (13), respectively. The first describes the matrix softening behavior [18], and the second corresponds to the Simplified Diverse Embedment Model (DEM) [19].

$$\sigma_{mat} = f_t e^{-cw_{cri}} \tag{12}$$

$$\sigma_{fib} = \alpha_f V_f K_{st} \tau_{f,max} \left(\frac{l_f}{d_f}\right)\left[1 - 2\left(\frac{w_{cr}}{l_f}\right)\right]^2 \tag{13}$$

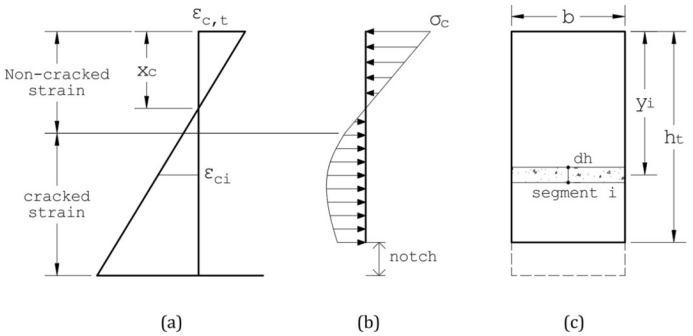

Figure 8 – Strain (a) and stress (b) diagram for the cross-section (c) analysis – Adapted from [17]

The displacement w_{crit} corresponds to the notch opening at a particular discretization segment i, obtained geometrically from Equation (14). In turn, f_t was initially estimated as $0.5\sqrt{f_{cm}}$ because of the lack of experimental data. The parameter c was set to 30, as recommended by [17], given that the UHPFRC produced by [13] did not include coarse aggregate.

$$w_{cri} = w_{cr,b}\left(\frac{y_i - x_c}{h - x_c}\right) \tag{14}$$

In Equation (13), the fiber volume ratio V_f is 2%, while the fiber length l_f and diameter d_f are 13 mm and 0.2 mm, respectively. The parameter α denotes the fiber orientation factor, assumed to be 0.5 [17], indicating that the fibers are partially aligned and exhibit a considerable degree of randomness in their orientation. Meanwhile, K_{st} represents a factor that accounts for the average pullout stress of the fibers, and it is computed according to Equation (15):

$$K_{st} = \begin{cases} \dfrac{\beta_f}{3}\dfrac{w_{cri}}{s_f}, & \text{for } w_{cri} < s_f \\ 1 - \sqrt{\dfrac{s_f}{w_{cri}}} + \dfrac{\beta_f}{3}\sqrt{\dfrac{s_f}{w_{cri}}}, & \text{for } w_{cri} \geq s_f \end{cases} \tag{15}$$

The parameter β_f represents for the fiber slip coefficient, as assumed to be 0.67, whereas s_f corresponds to the fiber slip associated with the pullout of a straight steel fiber, taken as 0.01 mm [17]. Finally, the pullout strength $\tau_{f,max}$ is the only unknown variable, initially assumed by calibration. Once the numerical load capacity of the prism P_{num} matches the experimental P_{exp}, the correct $\tau_{f,max}$ and, consequently, the proper σ-w_{cr} curve are obtained. Thus, The P_{num} is computed according to Equation (16):

$$P_{num} = \frac{4M_{max}}{L} \tag{16}$$

The σ-w_{cr} curves corresponding to the UHPFRC batches produced by [13] are shown in Figure 9, where the linearity limit represents the cracking strength f_t, and the peak stress corresponds to the tensile strength $f_{t,max}$. The softening curve presented in Figure 5 is obtained by converting the descending branch of the σ-w_{cr} curve into a stress-strain σ-ε relationship, using Equation (9).

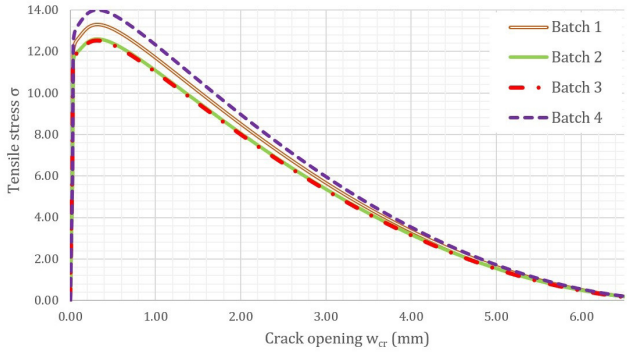

Figure 9 – Stress-crack displacement curves associated with the four batches produces by [13]

Once the σ-ε relationship in tension is determined, the load versus mid-span deflections for the beams tested by [13] are calculated and compared with the experimental data. The discrepancy between the charts is described by the coefficient of determination R^2, which represents the correlation between the experimental and numerical loads, with each pair associated with the same displacement δ.

For beams with two or more experimental datasets, all displacement domains associated with these sets were subdivided into segments of equal length Δδ, ensuring that the number of points generated for each curve is proportional to the extent of the displacement domain over which the comparison between the charts is valid.

Yang *et al*. [13] solely presented the experimental load-deflection *F-δ* curves of NR beams, R13 and R14-2. However, for R12-1 and R14-1, only the experimental moment-curvature *M-φ* relationship derived from *F-δ* data was provided. To validate the models for these beams as well, the experimental *F-δ* curve was back-calculated from the available *M-φ* relationship.

Regarding R22 and R23 beams, the experimental *F-δ* curves were not provided. Therefore, only the results obtained from the analytical method and via FEM analysis were compared.

2.3 Finite Element Modeling

This subsection describes the FEM modeling of the beams experimentally tested by Yang *et al.* [13], using the finite element software ABAQUS.

2.3.1 Material definition

Since the ascending branch of the stress-strain curve in compression is nearly linear, the behavior of UHPFRC was considered isotropic elastic, defined by the modulus of elasticity E_{cm} and the Poisson's ratio *v*, for stress levels below the compressive strength f_{cm}. In tension, the same assumption was applied for stress levels below the matrix cracking strength f_t. Given the absence of experimental data, *v* was assumed to be 0.2.

In turn, the nonlinear material behavior was represented by the concrete damage plasticity (CDP) model in ABAQUS, where the yield compressive and post-cracking tensile stresses relate to the inelastic ε_{in} and cracking ε_{cr} strains, respectively. Both ε_{in} and ε_{cr} are calculated from the total strain ε, as described by Equation (17):

$$\varepsilon_{in/cr} = \varepsilon - \left(\sigma / E_{cm}\right) \tag{17}$$

Provided that no cyclic loading tests were conducted, the damage parameter d_p used by ABAQUS to internally compute the plastic strain could be estimated as a function of the peak stress in both compression and tension [20], [21]. However, as this parameter is not incorporated into the proposed analytical method, it is likewise excluded from the FEM analysis to ensure a fair comparison between the results obtained from both approaches.

For the reinforcement, the bilinear idealized model presented in Figure 6 was used. The elastic behavior was defined by the Young's modulus E_s of 200 GPa and Poisson's ratio *v* of 0.3, whereas the plastic behavior in both compression and tension was defined by the yielding stresses of 500 and 540 MPa, associated with their respective plastic strains of 0 and 47.4‰.

The CDP model also requires the definition of a failure surface, which involves the calibration of the shape factor *K*, dilation angle Ψ, eccentricity ϵ, viscosity μ and ratio f_{b0}/f_{c0}.

The parameter *K* corresponds to the ratio of the second stress invariant on the tensile meridian to that on the compressive meridian, under the same hydrostatic pressure. This parameter influences the shape of the fracture surface, affecting its expansion and contraction relative to the standard Drucker-Prager's surface, as illustrated in Figure 10. In line with the literature ([20], [21]), *K* was adopted as 2/3.

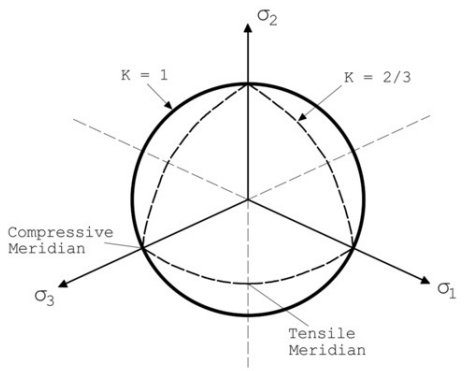

Figure 10 – Fracture surface in the deviatory plane – Adapted from [21]

In turn, the dilation angle Ψ refers to the inclination of the element as it deforms under an applied load, also indicating the degree of volumetric expansion under plastic deformation. In accordance with Jabbar *et al*. [21], Ψ was adopted as 35°. The eccentricity ϵ, for its part, denotes the rate at which the hyperbolic flow function approaches its asymptote, whose slope corresponds to the dilation angle Ψ, as illustrated in Figure 11. For the present study, the adopted ϵ value is 0.1, which is also the default parameter implemented in ABAQUS.

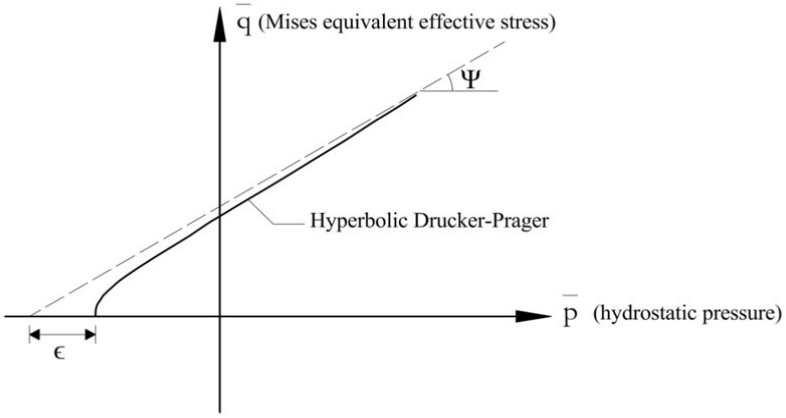

Figure 11 - Drucker-Prager hyperbolic plastic potential function from a meridian plane

Regarding the viscosity parameter μ, it introduces a small amount of artificial viscosity to smooth out variations in stress and strain during plastic deformation, helping to stabilize the solution by preventing localization and mesh sensitivity. A set of preliminary analyses was conducted for increasing values of μ, starting from zero in increments of 0.0005. The value of 0.002, identified as the minimum that avoided element distortion at midspan for a mesh size of 10 mm, was adopted as the reference value for all subsequent analyses.

Finally, the parameter f_{b0}/f_{c0} corresponds to the ratio of the effective compressive strength f_{b0} in biaxial state to its uniaxial compressive strength f_{c0}, reflecting how concrete behaves differently under biaxial stress compared to uniaxial stress. The default value in ABAQUS is 1.16, which was also adopted in the present study.

2.3.2 Interactions and boundary conditions

The interaction between the steel supports and the UHPFRC beam was modeled with normal behavior characterized by hard contact allowing separation after contact. For tangential behavior, a friction coefficient of 0.35 was applied. In turn, the interactions between the UHPFRC beam and the rebars were modelled using embedded region constraints.

A reference point was positioned at the center of the planar surface of the steel plates to define the boundary conditions. A vertical displacement of 30 mm was applied to the reference points of the upper steel plates, while a pinned boundary condition was assigned to the reference point on the lower plates. Additionally, in-plane displacements were constrained.

2.3.3 Discretization and meshing

The beam was modeled as a 3D solid and discretized into C3D8R finite elements, each having eight nodes with three degrees of freedom per node. The internal displacements are computed using linear interpolation functions and reduced integration. The supports were also modeled as 3D solids and discretized into C3D8R elements, whereas the reinforcement was divided into two-noded truss elements, with three degrees of freedom per node.

A sensitivity analysis was conducted for mesh sizes of 10, 20, 30, and 40 mm. The 20 mm mesh proved to be computationally efficient but resulted in some element distortion in high-strain regions. Although the 10 mm mesh was more time-consuming, it produced accurate results with minimal element distortion for a viscosity parameter μ of 0.002. Therefore, the 10 mm mesh size was adopted for the UHPFRC structural component.

Conversely, the mesh size adopted for the steel supports was 20 mm, which also corresponds to the length of the reinforcement truss elements. Figure 12 displays the undeformed shape of one of the beams analyzed in this study.

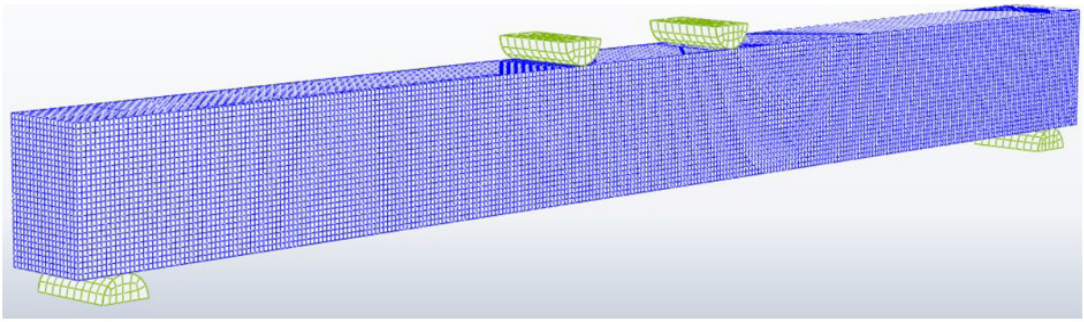

Figure 12 – Finite element model of the UHPFRC beam and steel supports

3 RESULTS AND DISCUSSION

This section presents the results of the experimental validation, with the analytical and numerical load-deflection curves plotted against the experimental results. First, the results for the NR beams are presented in Figure 13. The load-deflection curve obtained from the analytical method exhibited a coefficient of determination R^2 of 90.34% compared to the experimental curves, whereas the FEM analysis yielded an R^2 of 90.16%.

As illustrated by Figure 13, beam NR-1 experienced premature failure compared to NR-2, as well as the analytical and numerical predictions. This eventuality may be attributed to specific test conditions unique to NR-1. Despite identical casting procedures for both NR-1 and NR-2, where concrete was poured from the supports towards the midspan, the fiber distribution and orientation within the two beams may have varied, leading to different performances. This variation may be due to the casting procedure's conditions, which can have a significant influence on the structural member's response to the loading procedure.

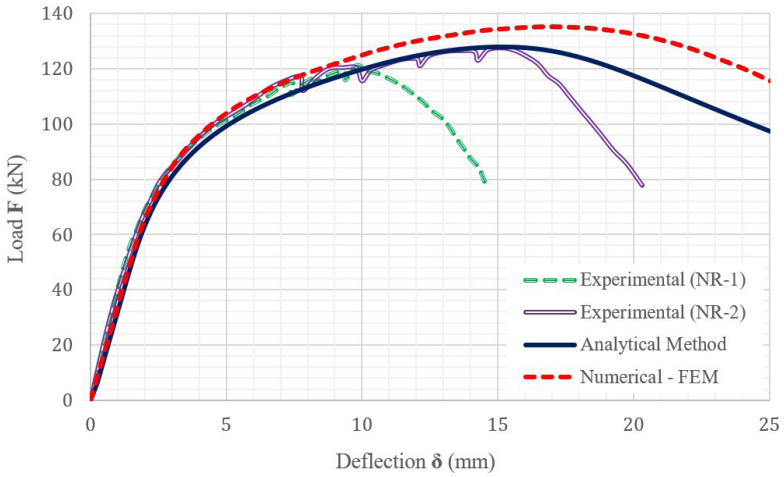

Figure 13 – Numerical load-deflection curves plotted against experimental results for NR beams

Additionally, it is possible that the distribution of fibers in NR-1 was not as well aligned with the direction of tensile stresses as the fibers in NR-2, for example. In addition, the perfect correspondence between the fiber orientation in the structural member and the orientation that occurs in the notched prisms tested by Yang *et al*. [13], for which the σ-ε relationship in tension was obtained via inverse analysis, is a very particular condition. For this reason, there are still many discussions about how the orientation factor should be considered in design codes [3]. Therefore, it is plausible to assume that beam NR-2 likely exhibited a more favorable fiber distribution than NR-1, more closely aligning with the idealized distribution predicted by the constitutive models, which resulted in better agreement between the experimental and predicted load-deflection curves. This also demonstrates that quality control during casting must be strictly observed when producing structural members with UHPFRC.

The absence of longitudinal reinforcement may also have played a crucial role in the significant differences observed in the load-deflection curves exhibited by both beams, making their flexural behavior totally dependent on the fiber reinforcement and its orientation as a result. The fiber content, along with its distribution and orientation, governs the post-cracking behavior of the structural elements and the propagation of cracks, ultimately leading to their eventual failure.

The presence of reinforcement could, for instance, delay crack propagation and alleviate stresses in the fibers, such that the ascending portion of the experimental F-δ curve would be more attributable to the capacity of the steel rebars to resist tensile stresses rather than to the fibers, whose distribution and orientation exhibit greater uncertainties.

Regarding R12 beams, the F-δ curves are shown in Figure 14. The coefficient R^2 associated with the analytical-experimental comparison corresponds to 91%, whereas that related to the FEM analysis is 87.2%. Unlike NR, the post-cracking analytical and numerical curves diverge significantly from those obtained experimentally, appearing to be about 29% stiffer compared to the experimental curves. This discrepancy may also be attributed to the casting procedures, which could result in poorer structural behavior than expected.

The experimental peak loads are also lower than those predicted by the models, suggesting that the concrete may not be exhibiting tensile hardening behavior or may be showing a much more modest performance compared to that idealized by the constitutive models. Since the hardening phase depends on the fiber orientation and arrangement [22], an assumption for the lower stiffness and premature failure is that the fibers in R12 were primarily oriented in directions different from those of the tensile stresses, even more unfavorably than those in NR beams, for which significant post-cracking convergence was observed. However, keeping the fibers aligned with the direction of the tensile stresses is challenging, especially for thick elements, as is the case in this study.

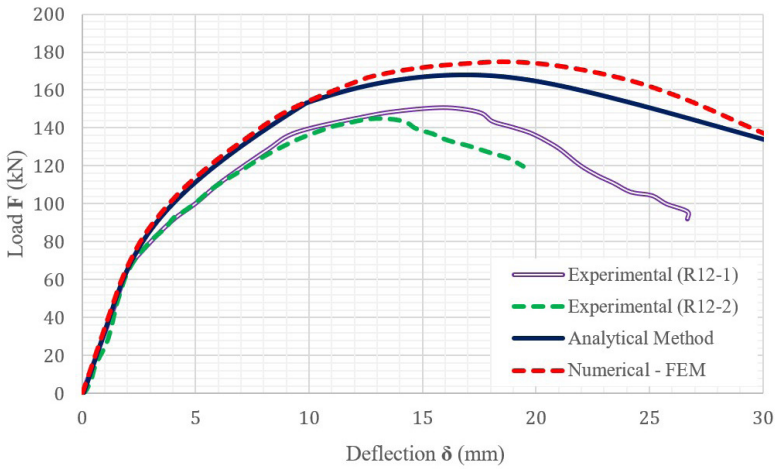

Figure 14 - Numerical load-deflection curves plotted against experimental results for R12 beams

Furthermore, the constitutive relations were obtained from the results of three-point bending tests on reduced-scale notched prisms. In this scenario, the fibers tend to align more easily in the flow direction, which is not the case for the evaluated beams with cross-section dimensions of 180 x 270 mm and a length of 2.9 m. Thus, a suggestion for further studies is to adjust the UHPFRC σ-ε relationship in tension to account for the casting procedures used in the structural element, so that the post-cracking behavior can be better represented.

Figure 15 displays the results associated with R13 beams, for which the R^2 values related to the analytical-experimental and numerical-experimental comparisons are 93.75% and 92.48%, respectively.

The post-cracking behavior of R13-1 was best represented by both analytical and numerical models, followed by R13-2. Nonetheless, R13C-1 exhibited a significant reduction in stiffness, with a peak load of approximately 15% lower than that predicted by the models. This behavior can be attributed to the casting procedures used for R13C-1, in which the concrete was placed at midspan and allowed to flow toward the supports. Such an important aspect is not accounted for by the constitutive relations used in the modeling, yet it also influences the fiber orientation and distribution. According to [13], this casting method promotes favorable fiber alignment – fibers aligned in the direction of the tensile stresses – only near the midspan, while leading to poor orientation in the shear spans.

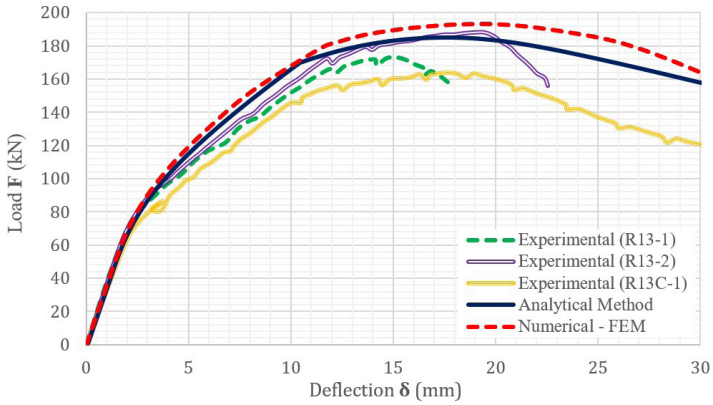

Figure 15 - Numerical load-deflection curves plotted against experimental results for R13 beams

Perhaps the favorable alignment at the center, where the tensile stresses are highest, contributed to preventing the sudden failure of the structural element. Unlike R13-1 and R13-2, the descending portion of the experimental *F-δ* curve extends to nearly 30 mm displacements, providing ductility to the member. Moreover, although not identical, the descending trend appears to be nearly parallel to those of the analytical and FEM models.

Therefore, it can be inferred that the fiber orientation at the midspan of R13C-1 is even more favorable than that of R13-1 and R13-2, which experienced sudden failure. Perhaps, if this orientation were consistent throughout the beam, there would likely be a higher probability of greater convergence between the experimental and predicted *F-δ* curves for R13C-1.

In turn, Figure 16 displays the results for R14 beams. The coefficient of determination R^2 related to the analytical-experimental and FEM-experimental comparisons corresponds to 98.45% and 98%, respectively. Similarly to R13C-1, the R14 beams did not exhibit sudden failure; this behavior may be associated with either a favorable fiber alignment near the midspan, the presence of four reinforcement rebars or even a combination of both.

Since the reinforcement ratio of the R14 beams is high compared to that of R12 and R13, a larger portion of the normal forces is carried by the steel rebars after cracking. Even if the fibers are unfavorably oriented, the rebars continue to bridge the cracks and prevent a sudden drop in load.

Additionally, since the contribution of fibers is lower relative to the reinforcement, uncertainties regarding their orientation do not cause significant deviations between the predicted and experimental responses, as observed in beams with low reinforcement ratios. This may explain the similarity between the experimental *F-δ* curves and the greater accuracy of both the analytical and numerical models in predicting the flexural behavior of the R14 beams, compared to the other elements.

Generally, both analytical and FEM models predicted a stiffer response compared to the experimental results. This can be attributed to the fact that concrete is not a homogeneous material, especially UHPFRC, for which fiber orientation and distribution depend strongly on the casting procedures. Furthermore, the models did not account for the shrinkage and microcracks that typically occur prior to the test, nor did they account for the fact that the bond between the steel rebars and the UHPFRC is not perfect, as assumed in the analyses.

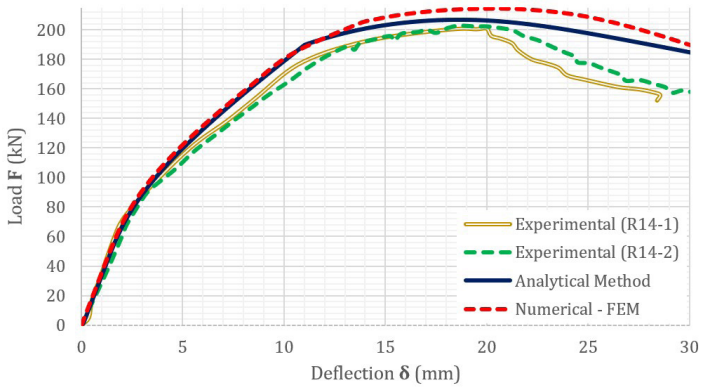

Figure 16 - Numerical load-deflection curves plotted against experimental results for R14 beams

Finally, Figures 17 and 18 display the load-deflection F-δ curves obtained from the proposed analytical method and FEM analysis for the R22 and R23 beams, respectively. The results show that the analytical and numerical models agree well, with coefficients of determination (R^2) of 99.6 and 99.8 for R22 and R23, respectively.

Nonetheless, the F-δ curves generated by the FEM models appear to be stiffer, especially for beams with low reinforcement ratios, as is the case for the NR and R12 beams. A possible hypothesis for this discrepancy may be related to the type of elements used for beam discretization and the mesh size. In addition, using reduced integration for the element type C3D8R may also affect the overall stiffness of the evaluated structural components [21].

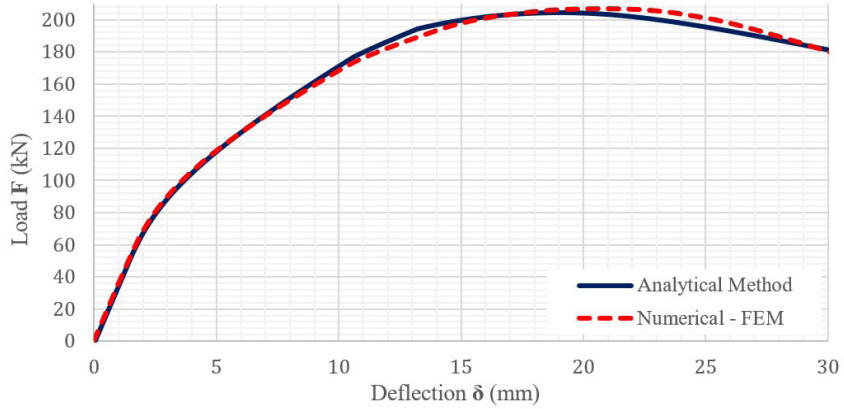

Figure 17 - Numerical load-deflection curves for R22 beams

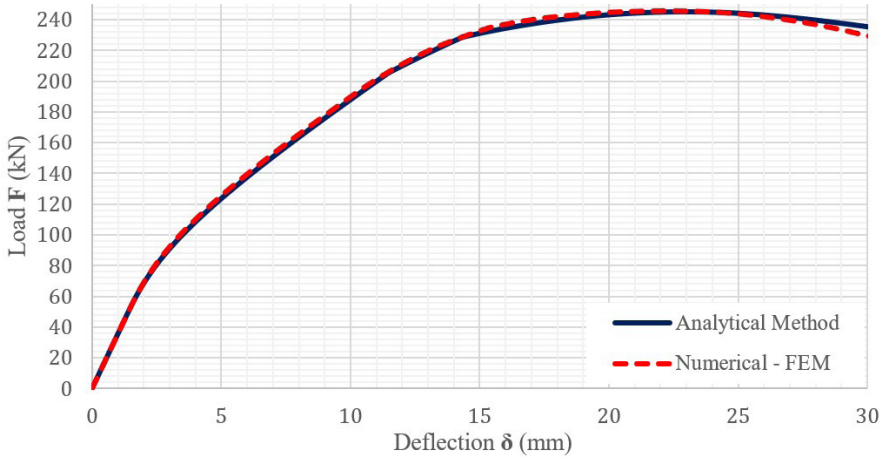

Figure 18 - Numerical load-deflection curves for R23 beams

4 CONCLUSIONS

This paper presents an analytical approach developed to predict the load-deflection response of reinforced UHPFRC beams under four-point loading. The method was based on the cross-sectional equilibrium of forces and compatibility of strains, which were used to determine the curvatures throughout the beams and then integrated to compute the corresponding deflections.

The load-deflection curves computed using the proposed method showed good agreement with the experimental results provided by Yang *et al.* [13], especially for service load levels below the steel yield limit. Less favorable results were obtained in the post-peak range and may be related to uncertainties regarding the orientation and distribution of fibers [3]. Thus, developing a constitutive model for the softening stage of the material, which accounts for these uncertainties, could contribute to a more realistic calculation of post-peak deflections using the proposed method.

Unlike methods that propose an average modulus of elasticity to account for stiffness variation along the beam, the proposed approach proved effective in determining point-by-point stiffnesses through the calculation of nodal curvatures. Additionally, a methodology based on the structural analysis of one-dimensional bar elements produced a response nearly identical to that provided by a 3D FEM model, combining accuracy with reduced computational time.

The similarity between the curves provided by the analytical model and the FEM analysis also demonstrates the efficacy of applying the principle of virtual work, commonly used for elastic analyses, to problems involving material nonlinearity and small deflections.

For future research, it is recommended that damage parameters be incorporated into the analytical model to provide a more precise assessment of the descending branch of the load-deflection curve, particularly for higher deflection levels than those considered in this study. In this context, it is also recommended that geometric nonlinearity effects be included, particularly for deflections that significantly exceed those typically considered in structural design.

It is further suggested that future studies explore variations in the fiber orientation factor αf within the Diverse Embedment Model [19] and determine different stress-strain relations for UHPFRC in tension, thereby generating load-deflection curves and evaluating their variation as a function of the fiber orientation factor. According to [23], fibers aligned in a preferential direction can lead to tensile strengths up to 90% higher than those of randomly distributed fibers.

The effects of shrinkage and temperature also require investigation. In a cross-sectional analysis, for instance, the strain at a given point can be expressed as the sum of stress-induced and shrinkage strains. Data available in the literature on UHPFRC shrinkage under different environmental conditions ([24], [25]) can be used in both analytical and numerical models to examine the influence of these parameters on the overall structural behavior.

5 REFERENCES

[1] M. Amran, S. S. Huang, A. M. Onaizi, N. Makul, H. S. Abdelgader, and T. Ozbakkaloglu, "Recent trends in ultra-high performance concrete (UHPC): Current status, challenges, and future prospects," *Constr. Build. Mater.*, vol. 352, pp. 129029, 2022.

[2] F. A. S. Barbosa, R. Serafini, A. D. de Figueiredo, and L. A. G. Bitencourt Jr., "Size effect on the flexural behavior of UHPFRC beams and RC beams strengthened with UHPFRC," *IBRACON Struct. Mater. J.*, vol. 18, no. 1, pp. e18113, 2025.

[3] M. M. Islam, Q. Zhang, and Q. Jin, "A review of existing codes and standards on design factors for UHPC placement and fiber orientation," *Constr. Build. Mater.*, vol. 345, pp. 128308, 2022.

[4] American Concrete Institute, *Building Code Requirements for Structural Concrete (ACI 318-15) and Commentary*. Farmington Hills: American Concrete Institute, 2015.

[5] D. Y. Yoo, N. Banthia, and Y. Yoon, "Predicting service deflection of ultra-high-performance fiber-reinforced concrete beams reinforced with GFRP bars," *Compos., Part B Eng.*, vol. 99, pp. 381–397, 2016.

[6] D. E. Branson, *Instantaneous and Time-Dependent Deflections on Simple and Continuous Reinforced Concrete Beams* (HPR Report 7). Montgomery: Alabama Highway Department, 1965.

[7] D. Gao, Z. Gu, J. Tang, and C. Zhang, "Fatigue performance and stress range modeling of SFRC beams with high-strength steel bars," *Eng. Struct.*, vol. 216, pp. 110706, 2020.

[8] D. Y. Yoo and Y. S. Yoon, "Structural performance of ultra-high-performance concrete beams with different steel fibers," *Eng. Struct.*, vol. 102, pp. 409–423, 2015.

[9] A. B. Sturm, P. Visintin, and D. J. Oehlers, "Blending fibres to enhance the flexural properties of UHPFRC beams," *Constr. Build. Mater. ASCE*, vol. 244, pp. 118–328, 2020.

[10] Y. Wang, X. Shao, J. Cao, X. Zhao, and M. Qiu, "Static and fatigue flexural performance of ultra-high-performance fiber reinforced concrete slabs," *Eng. Struct.*, vol. 231, pp. 111–728, 2021.

[11] F. Peng, Z. Fang, and S. Cui, "Deflection calculation for reinforced ultra-high-performance concrete beams based on effective moment of inertia," *Struct. J.*, vol. 119, no. 4, pp. 263–275, 2022.

[12] J. Lubliner, J. Oliver, S. Oller, and E. Oñate, "A plastic-damage model for concrete," *Int. J. Solids Struct.*, vol. 25, no. 3, pp. 299–326, 1989.

[13] I. H. Yang, C. Joh, and B. S. Kim, "Structural behavior of ultra high performance concrete beams subjected to bending," *Eng. Struct.*, vol. 32, no. 11, pp. 3478–3487, 2010.

[14] L. F. Martha, *Métodos Básicos de Análise de Estruturas*, 2. ed. São Paulo: LTC, 2017.

[15] W. A. Elsaigh, E. Kearsley, and J. M. Robberts, "Modelling the behavior of steel-fiber reinforced concrete ground slabs. I: development of material model," *J. Transp. Eng.*, vol. 137, no. 12, pp. 882–888, 2011.

[16] Association Française de Normalisation, *Concrete - Design, Calculation, and Detailing Rules for Ultra-High-Performance Fibre-Reinforced Concrete Structures*, NF P 18-710, 2016.

[17] S. C. Lee, H. B. Kim, and C. Joh, "Inverse analysis of UHPFRC beams with a notch to evaluate tensile behavior," *Adv. Mater. Sci. Eng.*, vol. 2017, pp. 1–10, 2017.

[18] J. Y. L. Voo and S. J. Foster, *Variable Engagement Model for Fibre Reinforced Concrete in Tension* (UNICIV Report R-420). Sidney: University of New South Wales, 2003.

[19] S. C. Lee, J. Y. Cho, and F. J. Vecchio, "Simplified diverse embedment model for steel fiber-reinforced concrete elements in tension," *ACI Mater. J.*, vol. 110, no. 4, pp. 403–412, 2013.

[20] T. E. T. Buttignol, E. C. Granato, T. N. Bittencourt, and L. A. G. Bitencourt Jr., "Experimental and numerical analyses of RC beams strengthened in compression with UHPFRC," *Struct. Eng. Mech.*, vol. 85, no. 4, pp. 511–529, 2023.

[21] A. M. Jabbar, L. S. Danha, and Q. A. Hasan, "Numerical simulation of ultra-high-performance concrete's compressive and tensile behaviour in beams," *J. Appl. Eng. Sci.*, vol. 21, no. 2, pp. 532–546, 2023.

[22] K. Wille, D. J. Kim, and A. E. Naaman, "Strain hardening UHPFRC with low fiber contents," *Mater. Struct.*, vol. 44, no. 3, pp. 583–598, 2011.

[23] H. Huang, X. Gao, and L. Teng, "Fiber alignment and its effect on mechanical properties of UHPC: An overview," *Constr. Build. Mater.*, vol. 296, pp. 123741, 2021.

[24] D. Y. Yoo, S. Kim, and M. J. Kim, "Comparative shrinkage behavior of ultra-high-performance fiber-reinforced concrete under ambient and heating curing conditions," *Constr. Build. Mater.*, vol. 162, pp. 406–419, 2018.

[25] Y. Zhang, L. Duan, H. Xin, and C. Wang, "Shrinkage behavior of ultra-high-performance concrete (UHPC) in cold winter conditions with shrinkage reducing agent (SRA) and expansive agent (EA)," *Constr. Build. Mater.*, vol. 436, pp. 136645, 2024.

Author contributions: FASB: conceptualization, data curation, formal analysis, methodology, writing - original draft; RS: data curation, formal analysis, methodology, writing - original draft; LAGBJ, RC and ADF: writing - review & editing, conceptualization, methodology, project administration, funding acquisition, supervision.

Editors: Bernardo Horowitz, Daniel Cardoso.